

Magnetic structures of an emerging flux region in the solar photosphere and chromosphere

Z. Xu^{1,2}, A. Lagg¹, and S. K. Solanki^{1,3}

¹ Max-Planck-Institut für Sonnensystemforschung, Max-Planck-Strasse 2, 37191 Katlenburg-Lindau, Germany
e-mail: xuzhi@ynao.ac.cn

² Yunnan Astronomical Observatory/National Astronomical Observatories, Chinese Academy of Science, Kunming 650011, PR China

³ School of Space Research, Kyung Hee University, Yongin, Gyeonggi 446-701, Korea

Received 2 September 2009 / Accepted 19 March 2010

ABSTRACT

Aims. We investigate the vector magnetic field and Doppler velocity in the photosphere and upper chromosphere of a young emerging flux region of the sun close to disk center.

Methods. Spectropolarimetric scans of a young active region made using the second generation Tenerife Infrared Polarimeter (TIP II) on the German Vacuum Tower Telescope (VTT) are analyzed. The scanned area contained multiple sunspots and an emerging flux region. An inversion based on the Milne-Eddington approximation was performed on the full Stokes vector of the chromospheric He I 10 830 Å and the photospheric Si I 10 827.1 Å lines. This provided the magnetic vector and line-of-sight velocity at each spatial point in both atmospheric layers.

Results. A clear difference is seen between the complex magnetic structure of the emerging flux region (EFR) in the photosphere and the much simpler structure in the upper chromosphere. The upper chromospheric structure is consistent with a set of emerging loops following elongated dark structures seen in the He I 10 830 Å triplet, similar to arch filament systems (AFS), while in the photosphere we infer the presence of U-loops within the emergence zone. Nonetheless, in general the upper chromospheric field has a similar linear relationship between inclination angle and field strength as the photospheric field: the field is weak (≈ 300 G) and horizontal in the emergence zone, but strong (up to 850 G) and more vertical near its edges. The field strength decreases from the photosphere to the upper chromosphere by approximately $0.1\text{--}0.2$ G km⁻¹ (or even less) within the emergence zone and by $0.3\text{--}0.6$ G km⁻¹ in sunspots located at its edge. We reconstructed the magnetic field in 3D based on the chromospheric vector field under the assumption that the He I 10 830 Å triplet forms along the magnetic field loops. The reconstructed loops are quite flat with supersonic downflows at both footpoints. Arguments and evidence for an enhanced formation height of He I 10 830 Å in arch-filaments seen in this line are provided, which support the validity of the reconstructed loops.

Conclusions. The main chromospheric properties of EFRs previously deduced for a single region NOAA 9451 are shown to be valid for another region as well, suggesting that the main original results may have a wider application. The main exception is that only the first region displayed a current sheet in the chromosphere. We propose a scenario in which the relatively complex photospheric structure evolves into the simpler chromospheric one.

Key words. Magnetic fields – Sun: chromosphere – Sun: infrared

1. Introduction

The solar magnetic field forming active regions is generated by means of a dynamo mechanism in the tachocline at the base of the solar convection zone around $r \approx 0.7 R_{\odot}$ (where r is the radial axis starting from the Sun's center, and R_{\odot} is the solar radius). Strong magnetic flux tubes escape from there due to magnetic buoyancy (Parker instability), travel through the convection zone, and finally emerge at the solar surface (Schüssler et al. 1994; Caligari et al. 1995; 1998; Fan 2004). The emerging field normally appears at the surface in the form of a bipolar region known as an emerging flux region (EFR), whose polarities, understood to be the footpoints of a loop system rising into the corona, separate at the photospheric level at speeds of less than 1 km s^{-1} (Strous et al. 1996; Strous & Zwaan 1999; Schmieder et al. 2004). Previous ground-based measurements of magnetic fields of EFRs focused mainly on the photosphere. Early observations using only Stokes I and V (Brants 1985a,b; Zwaan & Brants 1985) indicated that the emerging field has a strength

of a few hecto-Gauss, while modern full Stokes vector observations (Lites et al. 1998; Martínez Pillet et al. 1998; Kubo et al. 2003) find that during emergence the magnetic field is close to horizontal. A small-scale (less than $2''$) flux emergence event in quiet-sun internetwork was observed by the Hinode/Solar Optical Telescope (SOT) (e.g., Centeno et al. 2007) confirming the previous results of Martínez González et al. (2007) that flux emergence in the internetwork as small-scale loops is common. In the Hinode event, the authors found that the horizontal magnetic field appeared before any significant amount of vertical field become visible. A systematic analysis of these events was carried out by Martínez González & Bellot Rubio (2009). In addition, bipolar magnetic features are detected in the central part of EFRs near young sunspots. They were first reported by Bernasconi et al. (2002), who named them moving dipolar features (MDFs) to distinguish them from moving magnetic features (MMFs). Both types of features move horizontally at an average speed of around $0.3\text{--}0.5 \text{ km s}^{-1}$. However, MDFs flow toward sunspots and supergranule boundaries, in contrast

to MMFs, which move away from sunspots (Harvey & Harvey 1973; Lee 1992; Zhang et al. 2003). Both 3D MHD simulations and Hinode observations reveal an intricate pattern of often compact bipolar magnetic features between the two main magnetic polarities of the EFR (e.g., Cheung et al. 2007; 2008). The MDFs may be a special form of these bipolar features recorded by Hinode and seen in simulations.

In the chromosphere, the early research into EFRs concentrated on dynamic arch filament systems (AFS) in $H\alpha$ (Bruzek 1967, 1969, cf. the review by Chou 1993). At that time, the magnetic field could only be inferred morphologically from the line core observations of typical chromospheric lines such as $H\alpha$, or Ca II H and K. It is not straightforward to derive the physical conditions in the chromosphere from their profiles (e.g., Socas-Navarro & Uitenbroek 2004). The first direct measurement of magnetic vectors in an EFR in the upper chromosphere was presented by Solanki et al. (2003) and Lagg et al. (2004; 2007) based on full Stokes I , Q , U , and V profiles of the He I 10830 Å triplet. The observations of NOAA 9451 detected two magnetic features: a set of rising magnetic loops and an electric current sheet. So far NOAA 9451, observed in 2001, is the only EFR whose chromospheric magnetic field has been analyzed.

The He I 10830 Å triplet is a unique tool for investigating the magnetic structures of the upper chromosphere (e.g., see the reviews by Lagg 2007; Trujillo Bueno 2009). It originates from the transition between the two lowest metastable energy levels of Orthohelium, $1s2s\ ^3S_1-1s2p\ ^3P_{0,1,2}$ (de Jager et al. 1966). The lower levels of the transition are understood to be populated primarily by recombination of singly ionized helium previously ionized by the EUV irradiance from the corona (Pozhalova 1988; Avrett et al. 1994; Andretta & Jones 1997; Centeno et al. 2008). Penn & Kuhn (1995), Rüedi et al. (1995; 1996) and Lin et al. (1998) pointed out that because of its sensitivity to the Zeeman effect and that it is narrow compared to other chromospheric lines, it is feasible to use He I 10830 Å to investigate the full magnetic vector in the upper chromosphere. Furthermore, Trujillo Bueno et al. (2002) showed that in weakly magnetized plasma structures the linear polarization of the He I triplet is dominated by atomic level polarization, even in forward scattering geometry. In the presence of a magnetic field inclined with respect to the local solar vertical direction, this atomic level polarization (and the ensuing emergent Stokes Q and U profiles) is modified by the Hanle effect, which, together with the Stokes V signals that the Zeeman effect induces, has been used to infer the magnetic field in chromospheric spicules (Trujillo Bueno et al. 2005) and in a polar crown prominence (Merenda et al. 2006). As shown below, the upper chromosphere of the emergence zone (i.e., between the footpoints of EFRs) is usually pervaded by weak and horizontal magnetic fields, which tend to produce linear polarization profiles with shapes similar to those investigated by Trujillo Bueno et al. (2002) in a coronal filament at the solar disk center. However, as shown by Trujillo Bueno & Asensio Ramos (2007), for magnetic field strengths $100 < B < 2000$ G the linear polarization of the He I triplet is generally caused by the joint actions of atomic level polarization and the transverse Zeeman effect, while the circular polarization is always dominated by the longitudinal Zeeman effect. For stronger fields, the linear polarization of the He I triplet is dominated by the transverse Zeeman effect.

In the present paper, we present the analysis of data from another young emerging flux region NOAA 10917 observed in 2006. A comparison with the results obtained from NOAA 9451 may help us to distinguish between features peculiar to each

region and common to the chromospheric magnetic field of EFRs. The present set of observations display distinct advantages compared with the data of NOAA 9451 due to the improved spatial sampling and coverage provided by the second generation Tenerife Infrared Polarimeter (TIP II, Collados et al. 2007), and that different parts of an emerging loop were recorded nearly simultaneously. Other improvements are the inclusion of the Paschen-Back effect in the inversion and the resolution of the 180° azimuth ambiguity problem, for which we here use the non-potential magnetic field calculation (NPFC) method of Georgoulis (2005).

The interpretation favored by Solanki et al. (2003) of the height at which the young loop-like structures are sampled by the He I line was questioned by Judge (2009). He proposed instead that the field in these structures be measured at a nearly constant height. In this paper, we provide arguments that support the original interpretation of Solanki et al. (2003, see Sect. 6.3).

The following is an outline of the present paper: in Sect. 2, the observations are presented, while Sect. 3 introduces the inversion code and the atmospheric model used for the data analysis. The main features of the retrieved magnetic field in the local solar frame and the LOS velocity field are presented and analyzed by comparing the photosphere and upper chromosphere in Sect. 4. In Sect. 5, we reconstruct magnetic loops in 3 dimensions based on the retrieved chromospheric vector field and the assumption that the He I triplet forms along magnetic field loops. Finally, the results are discussed in Sect. 6 and conclusions are given in Sect. 7.

2. Observations

The active region NOAA 10917 first appeared on 20 October 2006 as a simple pore with a positive polarity. The pore grew considerably in the following 24 h, developing a penumbra and becoming a sunspot. Several pairs of pores with mutually opposite polarities began to emerge on 21 Oct., when the region was located at 05°S , 30°W , which corresponds to $\mu = \cos\theta = 0.87$ (θ is the heliocentric angle, i.e., the angle between the local solar surface normal direction and the line-of-sight direction). Three of these newly emerged pores went on to become sunspots as well. The development of this region on this date is illustrated in Fig. 1, showing parts of full-disk continuum images recorded by SOHO/Michelson Doppler Imager (MDI, Scherrer et al. 1995).

Spectropolarimetric observations were carried out using TIP II (Collados et al. 2007) at the German Vacuum Tower Telescope (VTT), and by performing digital slit-jaw filter recordings in $H\alpha$ and Ca II K from 13:24 UT to 16:51 UT on 21 Oct. 2006. In attempting to simultaneously observe the different parts of freshly emerged loops, the spectrograph entrance slit was placed parallel to the dark fibrils seen in the $H\alpha$ slit-jaw images. The slit was $78''$ long and the pixel size was $0.175''$. The whole active region was scanned with a $0.35''$ step size. The slit orientation and scan direction are indicated in Fig. 1 (lower right panel). At each scan position, the full Stokes vector was recorded with a spectral resolution of $11\text{ m}\text{\AA}$. The 11 \AA wide spectral window contained the chromospheric He I 10830 Å triplet as well as the photospheric Si I 10827.1 Å line. Both are sensitive to the Zeeman effect. Having spectra of both lines allows us to study the magnetic vector co-spatially and co-temporally in two different atmospheric layers.

Panels a-d of Fig. 2 display the observed region viewed in the infrared continuum (10825 \AA), Ca II K line core, $H\alpha$ line core and intensity integrated over the He I 10830 Å triplet around

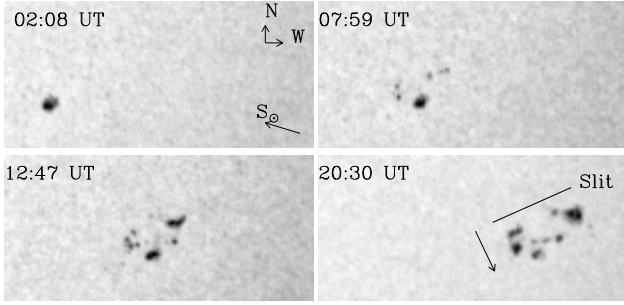


Fig. 1. Development of the active region NOAA 10917 on 21 October 2006 seen in continuum radiation (SOHO/MDI). The solar coordinates and the disk center position are indicated in the *top-left panel*. The slit orientation (a stick marked “slit”) and the scan direction of the spectropolarimetric observations (an arrow) are indicated in the *bottom-right panel*.

16:28 UT. Two main features of EFRs can be clearly seen: compact bright plages in Ca II K and an arch filament system (AFS) with bright points near the footpoints in H α . Structures resembling the AFS are seen in the He I line, the three filaments being oriented nearly parallel to the slit showing a good correspondence to those detected in H α . The rightmost structure (more inclined relative to the slit) is seen as a strong absorption feature only in the He I line. These structures were present during the whole sequence of observation from 13:24 to 16:51 UT. The transition region and coronal context of NOAA 10917 is presented in Figs. 2e and f, which show images in the 304 Å and 171 Å channels of the SOHO/Extreme-ultraviolet Imaging Telescope (EIT, Delaboudinière et al. 1995). The 304 Å channel is chosen since it is dominated by emission from He II, while the 171 Å channel is selected because it represents the cool corona and may show more similarities to the He I line than the hotter 195 Å and 284 Å channels. We find that this is an isolated active region, in which the spots, pores (indicated by the yellow contour from MDI), and most of the plage are located within the scanned area. In addition, the loops visible in 171 Å as bright ridges terminate mainly in the footpoints located within the scanned region.

Two different sets of observations of NOAA 10917 on 21 Oct. 2006 were performed. We first made 15 scans of a subregion with a field-of-view of 15 Mm \times 55 Mm, the time series of which spans 74 min from 13:24 to 14:38 UT. We then performed a single long scan, covering a field-of-view of 50 Mm \times 55 Mm and lasting from 16:28 to 16:51 UT. The exposure time per scan position was 7 s, resulting in a noise level of typically $5 \times 10^{-4} I_c$. The estimated spatial resolution of the image was limited by the seeing to roughly 1.5". We applied the standard TIP data reduction routines, which include dark current subtraction, flat-fielding, and polarimetric correction including an automated cross-talk removing algorithm (Beck et al. 2005). An accurate continuum correction was performed by comparing the average flat field profile with the FTS spectrum. The quiet-Sun Stokes I profile, computed by averaging 100 profiles with the lowest polarization signal in the observed map, was used to determine the wavelength calibration by assuming that the core position of the photospheric spectral lines correspond to the laboratory wavelengths. To enhance the signal-to-noise ratio, we applied a 5-pixel binning along the wavelength axis, resulting in a wavelength resolution of 55 mÅ per pixel. In addition, a 2-pixel binning along the slit direction was applied, resulting in a quadratic pixel size of 0.35 arcsec².

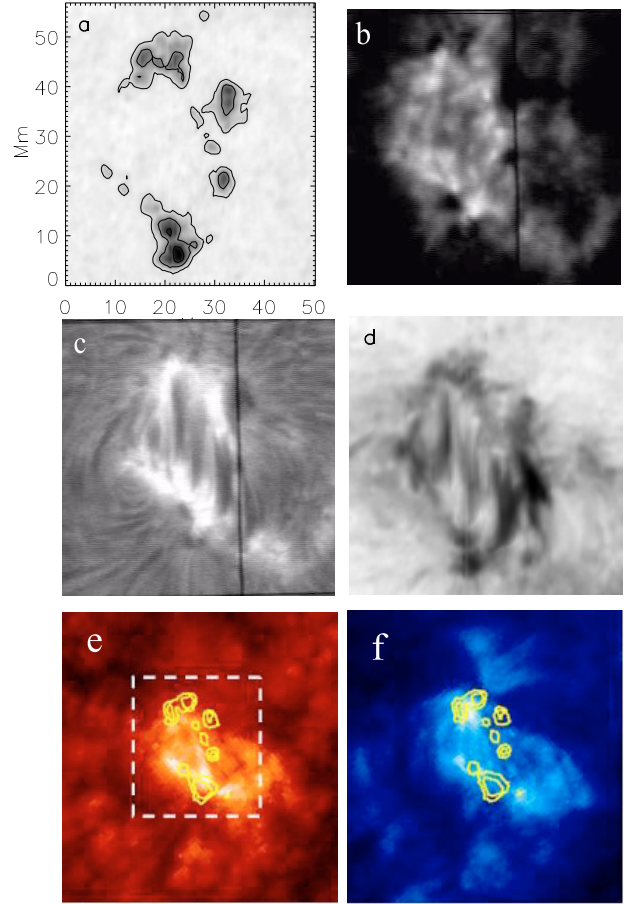


Fig. 2. a): morphology of NOAA 10917 on 21 Oct. 2006 viewed in infrared continuum radiation at 10825 Å, b): the Ca II K line core, c): the H α line core, and d): in the He I 10830 Å line (intensity integrated from 10830.0 to 10830.6 Å) around 16:28 UT. Panels b) and c) display slit-jaw images. The position of the slit at the time these images were recorded is visible as a vertical black line. The images in panels a) and d) have been put together from the scan made by the slit, so that the left and right parts of the images refer to different times. e)-f): extreme ultraviolet passbands centered on 304 Å and 171 Å of SOHO/EIT around 13:30 UT, superimposed on the contours (thick yellow lines) of the SOHO/MDI continuum image recorded at 20:30 UT. The continuum image at 20:30 UT is selected because the sunspot distribution is most similar to our ground-based observation at 16:28 UT. Panels e) and f) cover a larger field of view. The dashed box in panel e) outlines the field of view of panels a)-d).

3. Data analysis

Full Stokes I , Q , U , and V profiles of both Si I and He I lines were fitted using the HeLiX code (Lagg et al. 2004), which is based on the Unno-Rachkowsky analytic solution of the radiative transfer equation for polarized radiation in a Milne-Eddington model atmosphere. The code obtains the best fit of the observed profiles by varying eight free parameters for a given atmospheric component: the strength of the magnetic field vector (B), its inclination (γ) and azimuth angle (χ), line-of-sight velocity (v_{los}), Doppler width ($\Delta\lambda_D$), damping constant (a), slope of the source function (S_1), and the opacity ratio between line-center and continuum (η_0). The code allows the parameters to be retrieved for more than one atmospheric component simultaneously, to treat the presence of unresolved structures within a spatial resolution element, or light scattered into it from outside the resolution element. An additional free parameter, the filling

factor, f_i , is used to fix the relative weight of each component, where $\sum f_i = 1$ (i indicating each component to be considered).

For the Si I line, we used a two-component atmospheric model composed of a magnetic component and a field-free one. The latter represents both the contribution to Stokes I from the field-free material in the resolution element and the straylight induced contamination of the Stokes I originating in the surrounding regions.

At the formation level of the He I line in the upper chromosphere, we can safely assume that the magnetic field fills the resolution element completely due to the strong expansion of the field in the lower chromosphere (e.g. Solanki & Steiner 1990), so we generally used a one-magnetic-component atmospheric model. However, to fit the profiles at some locations two magnetic components were needed because of the presence of multiple line-profile components within one resolution element, each with a different Doppler shift (Lagg et al. 2007; Aznar Cuadrado et al. 2007). We used the following approach. First we applied a one-component inversion to the whole observed region, followed by the two-component model inversion. We then compared their fit quality, which is represented by a “fitness” parameter (see Eqs. (1) and (2) of Lagg et al. 2007, for the definition) provided by the Pikaia genetic algorithm (Charbonneau 1995). The two-component model was considered to be necessary only when the quality of the fit, i.e., the fitness parameter, was increased by at least 20% with respect to the one-component fit. For our data, the fraction of pixels for which a 2-component model was needed is about 12.5%. In the two-component model, we initially kept the S_1 , $\Delta\lambda_D$, and the magnetic field vector (B , γ , and χ) the same in both atmospheric components. Whenever the quality of the fit was compromised by this, which was the case for only a few pixels, we employed a two-component model with independent magnetic field strength (B) to obtain a good fit. An example is displayed in Fig. 3. In this pixel, the same magnetic field strength in both magnetic components was unable to reproduce the Stokes V profile around 10831.5 Å very well. The difference in the quality of the fits when we assume independent or identical field strengths for the two components is similar to that shown in Fig. 4 of Lagg et al. (2007). In Fig. 3, one component displays subsonic flows (sound speed ≈ 10 km s $^{-1}$ in the chromosphere), the other exhibits supersonic redshifts. This agrees with the results of Aznar Cuadrado et al. (2005), who found that supersonic downflows are rather common in the solar upper chromosphere. We therefore refer to the two components as the subsonic (or rest) and the supersonic ones.

The version of HeLIx employed here takes into account the incomplete Paschen-Back effect (Socas-Navarro et al. 2004; Sasso et al. 2006) and Hanle effect when calculating the He I triplet. The Hanle effect is treated with a simplified approach in a forward scattering geometry (Collados et al. 2003; Lagg et al. 2004). We believe that this simplification is reasonable to interpret our observation of NOAA 10917, even though the line-of-sight corresponds to $\mu = 0.87$ (cf., the curves with $\mu = 0.9$ in Fig. 9 of Asensio Ramos et al. 2008). An example of linear polarization caused by the scattering polarization and its modification due to the Hanle effect is shown in Fig. 4. Here the Stokes U profile is clearly influenced by both the Zeeman and Hanle effects, but the signal produced by atomic level polarization fully dominates.

Finally, we resolve the 180° ambiguity in the magnetic azimuth for the magnetic field in the photosphere and upper chromosphere. By using the non-potential magnetic field calculation method, NPFC (Georgoulis 2005 – see also Metcalf et al. (2006

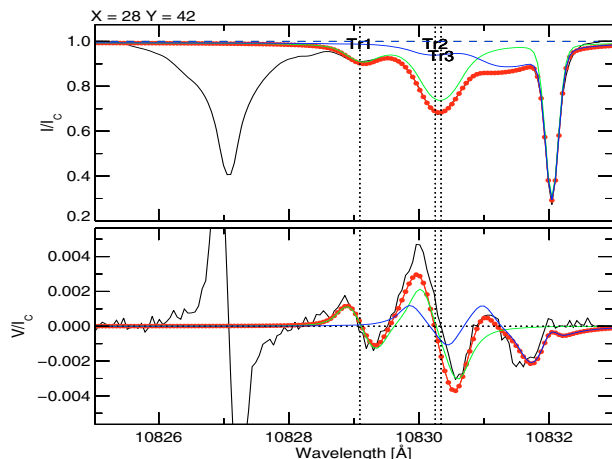


Fig. 3. Stokes profiles of the pixel located at $X = 28$, $Y = 42$ in the coordinates of Fig. 2a. Two atmospheric components coexist and cause the partial overlap of line profiles of the He I triplet and the telluric line at 10832 Å. The observed profile is shown in black (solid line), the best fit is shown in red (filled circles). Three vertical dotted lines indicate the line-center rest positions of the He I triplet. The fit is the sum of two components: the one nearly at rest is plotted in green ($B = 220$ G, $V_{\text{los}} = 1.3$ km s $^{-1}$) and the supersonic red-shifted one in blue ($B = 460$ G, $V_{\text{los}} = 29$ km s $^{-1}$). The telluric line is fitted using a Voigt profile.

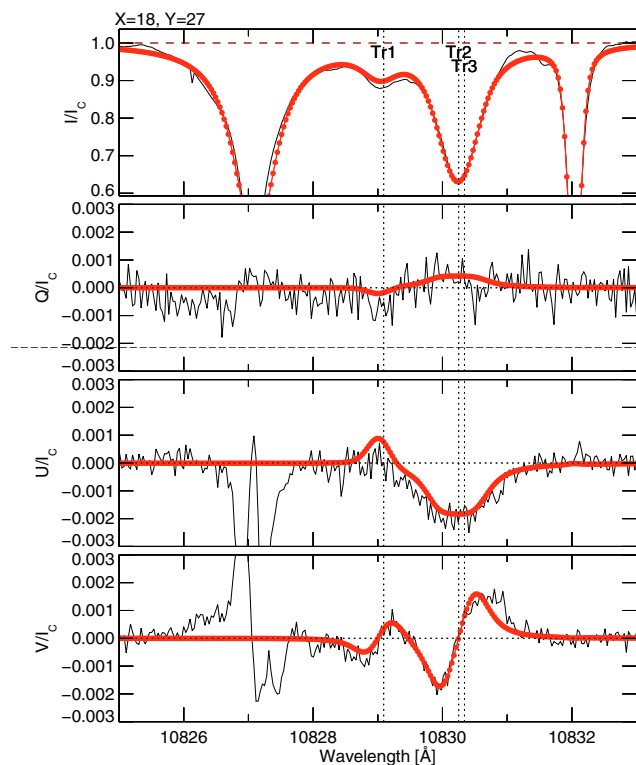


Fig. 4. Stokes profiles of three-pixel average at $X = 18$, $Y = 27$ in the coordinates of Fig. 2a. A combination of the Hanle and Zeeman effects acting in a single atmospheric component reproduce both the linear and circular polarization profiles in He I line. We perform a Hanle-slab inversion for this point and the inferred magnetic field vector in the local solar frame is $B = 360$ G, $\gamma = 112^\circ$, $\chi = 72^\circ$ ($\chi = \pm 90^\circ$ is along the slit direction). More details of the Hanle-slab model application at the loop top are given in Sect. 6.3. The black and red curves, as well as the dotted vertical lines, have the same meaning as in Fig. 3. No fit was made to Stokes Q , U , and V of the Si I line.

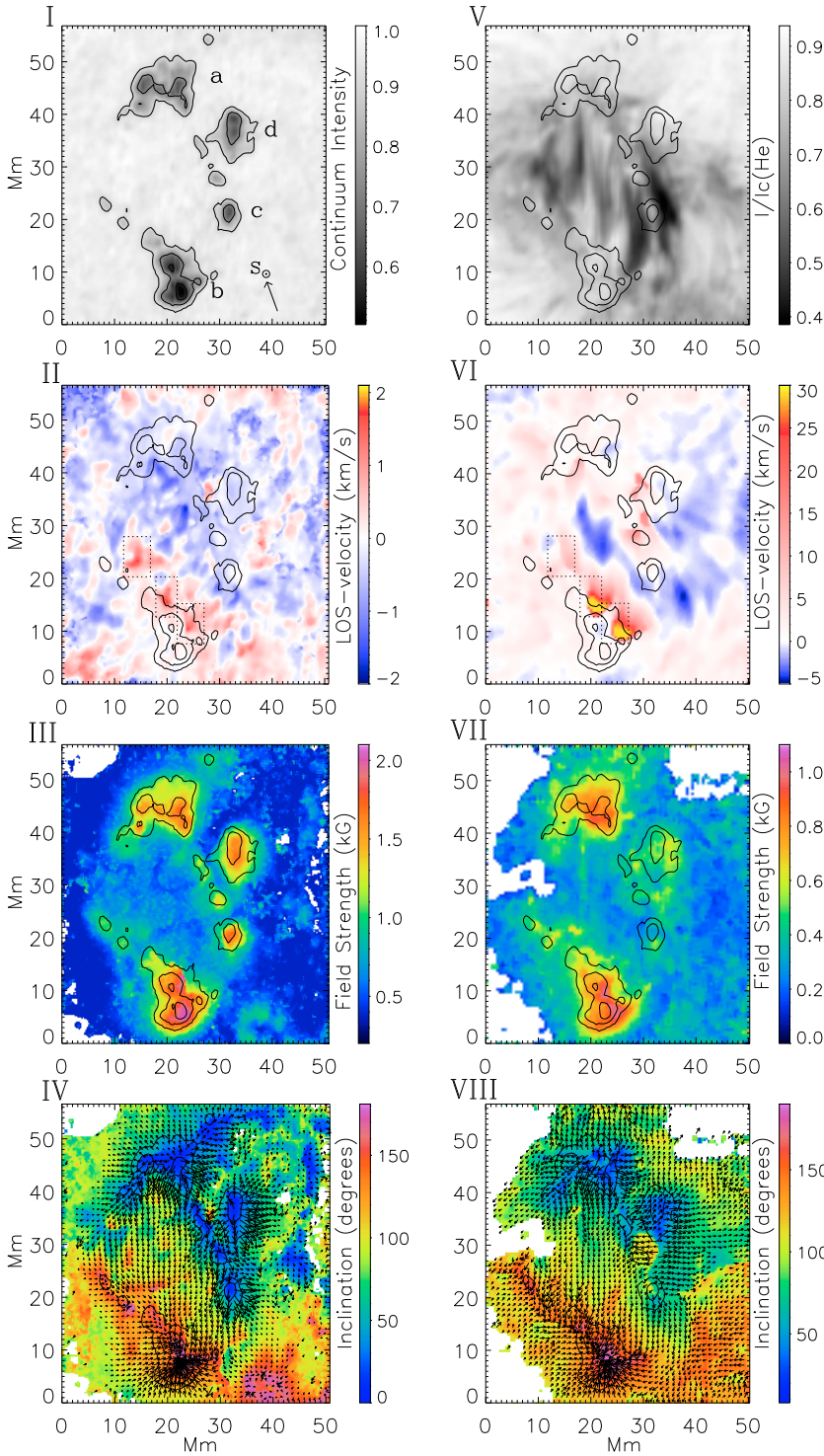


Fig. 5. Retrieved atmospheric parameters of active region NOAA 10917 (21 Oct. 2006, 16:28–16:51 UT) in the photosphere (*left column*) and the upper chromosphere (*right column*). **I:** the infrared continuum intensity, with the direction toward solar disk center, S_{\odot} , marked by an arrow. Sunspots a-d discussed in the main text are identified. **V:** the intensity ratio of the He I line core to the continuum. **II & VI:** the LOS velocity (positive = redshift). The dotted boxes outline the co-locations of the photospheric downflows of around 1.5 km s^{-1} with supersonic downflows in the upper chromosphere (see text). **III & VII:** the magnetic field strength. **IV & VIII:** the azimuth angle (arrows) superimposed onto the magnetic field inclination angle (to the local vertical direction; colors) in the local solar frame (see text). The contour lines in each panel indicate the sunspots, while blank areas are regions where the polarization signals are below a given threshold (given by $\sqrt{Q^2 + U^2 + V^2}/I_c = 10^{-3}$) and are not inverted.

for a comparative evaluation with other disambiguation codes), we convert the magnetic field vector into the local reference frame. The algorithm self-consistently calculates the potential and non-potential magnetic field vectors whose superimposition most precisely describes the studied vector magnetic field observations.

4. Results

By inverting the Si I and He I profiles of the whole observed region, we obtained the atmospheric parameters for each spatial point, in both the photosphere and upper chromosphere.

The retrieved maps of the parameters in the active region NOAA 10917 are shown in Fig. 5. In addition to the infrared continuum and He I line core intensity, we plot the LOS velocity and the magnetic vector in the photosphere and upper chromosphere, respectively.

The plotted magnetic vectors have been transformed into the local solar frame and are represented as if viewed from radially above. Despite considerable effort being invested in solving the 180° ambiguity, we remain unsure whether we have obtained the correct solution for the whole field of view in both layers. In particular in the upper chromosphere, where the retrieved magnetic vectors are more noisy in the LOS frame, we found some

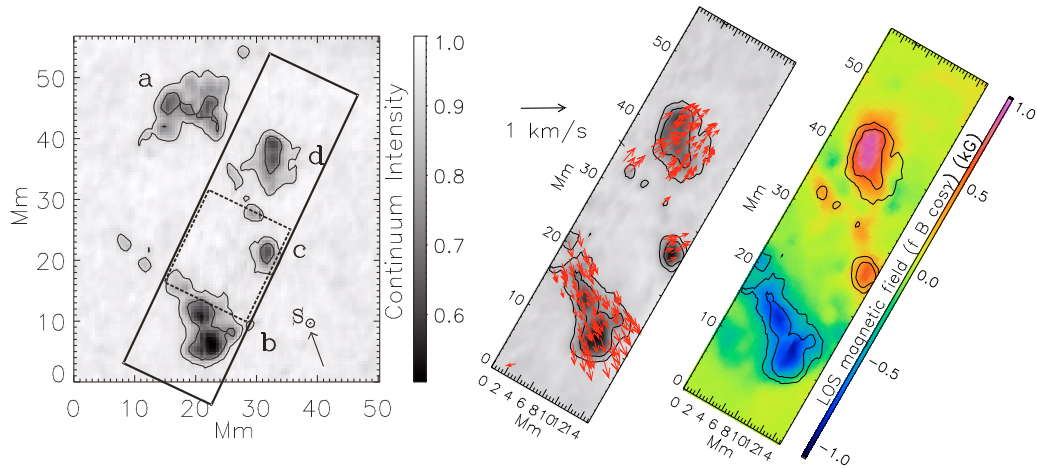


Fig. 6. Horizontal movement of the sunspots and pores in the course of the observation. *Left:* continuum image of the whole active region. The solid-line rectangle outlines the field of view of the 15 successive short scans from 13:24 to 14:38 UT. The arrow points to disk center. The dotted square displays the area shown in Fig. 9. *Middle:* the flow field derived from the displacement of sunspots and pores inside the rectangle of the left panel (overplotted arrows). The length of the arrow above this frame corresponds to a speed of 1 km s^{-1} . The continuum image was obtained halfway through the time series (14:00 UT) and the position of sunspots and pores at that time is marked by contours. *Right:* the pixel-averaged longitudinal magnetic field flux $fB \cos \gamma$ (see the main text).

artifacts (e.g., around $x = 30$, $y = 30$ in Fig. 5_VIII). However, we believe that at worst the ambiguity was incorrectly resolved mainly at the edge of the EFR. This should not affect our conclusions.

The plotted LOS velocity in the photosphere corresponds to that of the magnetic component. In the upper chromosphere, when a two-magnetic-component model is employed, the plotted LOS velocity is weighted by the filling factor of each component (i.e. $V_{\text{los}} = V_{1,\text{los}}f_1 + V_{2,\text{los}}f_2$).

Sunspots in this region are identified in Fig. 5_I. One day before our observation only sunspot d was present. Sunspot a, b, and c formed in the intervening time. The young sunspots a, b, and their surrounding pores appear to be connected in the upper chromosphere by a series of long dark fibrils seen in the He I line core image (Fig. 5_V). The recently formed sunspots a, b and c are footpoints of relatively freshly emerged flux loops. They roughly encircle the so-called emerging flux zone.

4.1. Velocity field in the photosphere and upper chromosphere

The LOS velocity in the upper chromosphere is presented in Fig. 5_VI. Upflows of up to 4 km s^{-1} are found between spot a and b, i.e. at a place where we expect the tops of the freshly emerged magnetic loops to lie. Redshifts are present on both sides of this central stripe of blueshifts, i.e. where we expect the loop legs. Redshifts smoothly increase with distance along the legs, and become supersonic at some locations. For instance, supersonic downflows with a maximum value exceeding 30 km s^{-1} are found around the preceding sunspot b. These supersonic downflows can have a filling factor as high as 0.8. Both the intensity image and the magnetic field structure support the conclusion that the supersonic downflows very likely end within this sunspot. The photospheric velocity map is shown in Fig. 5_II. The flow field does not resemble the chromospheric one. However, in contrast to the findings of Lagg et al. (2007) for NOAA 9451, we observe photospheric downflows of 1.5 km s^{-1} below the supersonic chromospheric downflows. The positions of these photospheric flows are marked by dotted boxes in Fig. 5_II and VI. In some regions, the supersonic

downflows are present in an atmospheric component with only a small filling factor. These locations appear unremarkable in this plot, which shows a filling-factor-weighted LOS velocity.

We also determined the transversal motion (to the LOS) of dark features in the photosphere based on 15 repeated scans over 74 min covering a limited FOV. The field of view of these repeated scans is marked by a solid rectangle in the left panel of Fig. 6. The flow field is derived from the displacement of dark objects (sunspots and pores) by local correlation tracking (LCT, November & Simon 1988) and is indicated in the middle panel of Fig. 6 by red arrows. The opposite polarity spots and pores obviously appear to be separating away from each other (see middle & right panel of Fig. 6), but not radially. The presence of a shear component to their motion is evident. The transversal velocity of sunspot b reaches 0.4 km s^{-1} . Unfortunately, the field-of-view is insufficiently large to cover the following sunspot a, hence our knowledge of the transversal motion of this active region remains incomplete.

4.2. Magnetic field in the photosphere and upper chromosphere

A comparison of Fig. 5_III with 5_IV and of Fig. 5_VII with 5_VIII appears to show that there is a correlation between the inclination and strength of the 4-pixel averaged magnetic field in both the photosphere and the chromosphere. This is shown more quantitatively in Fig. 7, in which the field inclination angle is plotted as a function of the field strength of sunspots (here including pores) and the emergence zone in both layers. We distinguish the sunspots by red and the emergence zone by black plus symbols. Points lying within the outer contour in Fig. 5_I are assigned to sunspots, while the emergence zone is the area encircled by the sunspots or pores. We find the following: (1) Both the photosphere and upper chromosphere exhibit a weak, horizontal magnetic field in the emergence zone. Field strength and inclination are roughly linearly related in both atmospheric layers, the strongest, nearly vertical fields being found in sunspot umbrae. In the sunspots (indicated by red plus signs in Fig. 7), the chromospheric field is more horizontal than the photospheric one. Comparing the two panels of Fig. 7, we

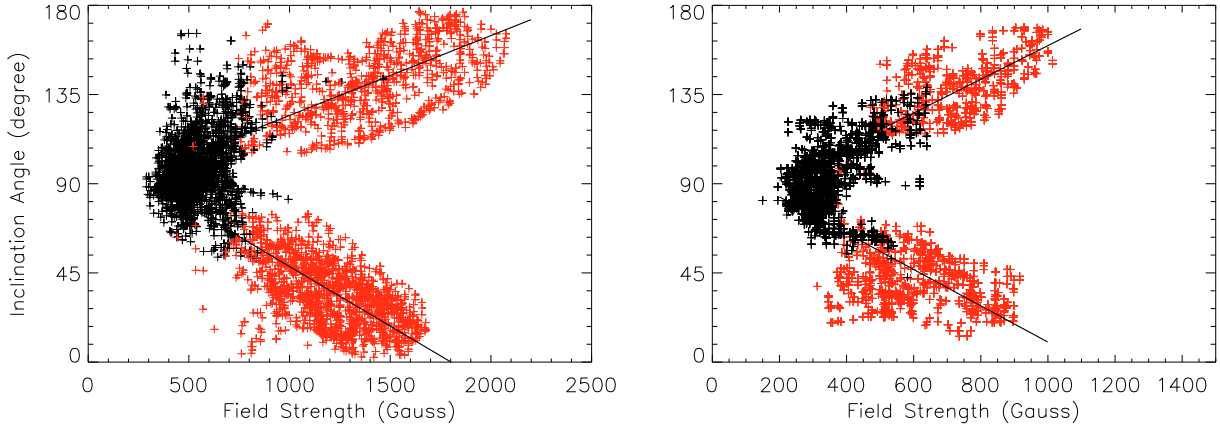


Fig. 7. Scatter plots of pixel-averaged inclination angle versus magnetic field strength in the photosphere (*left*) and the upper chromosphere (*right*) for the region shown in Fig. 5. Red symbols represent the sunspot (or pores) and black symbols the emergence zone encircled by sunspots and pores.

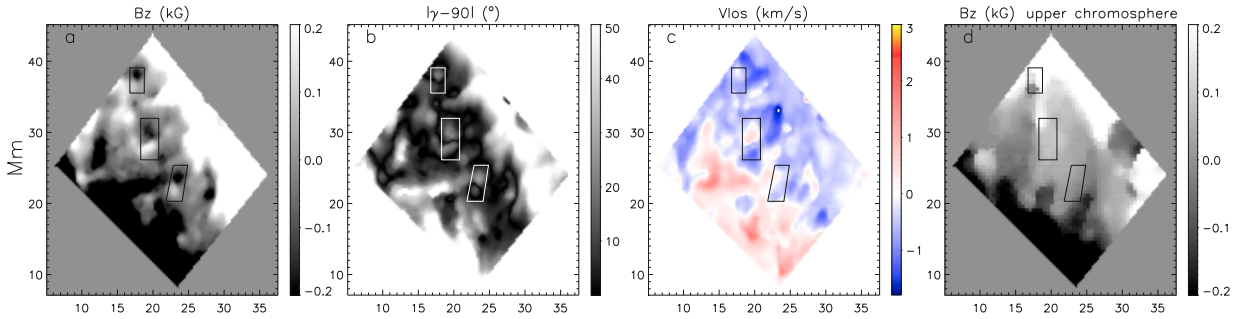


Fig. 8. **a–c**): pixel-averaged vertical magnetic field, field inclination with respect to the solar surface (see text), and LOS velocities in the photosphere. **d**): pixel-averaged vertical magnetic field in the upper chromosphere. In panels **a**) and **d**), white (dark) shading refers to the positive (negative) polarity. In panel **b**) dark (white) patches indicate that the field is parallel (inclined) to the solar surface. In panel **c**), downflows are positive. The coordinates are the same as in Fig. 5.

note that the chromospheric and photospheric fields display a qualitatively similar behavior, but with the data points shifted to the weaker fields in the chromosphere. Regression lines placed separately through the points with inclination $\leq 90^\circ$ and those with inclination $> 90^\circ$ are also shown in the figure. The average unsigned slope to the chromospheric points, 0.088, is a factor of 1.76 larger than the corresponding photospheric quantity. In addition, the magnetic azimuth angle in both layers is similar (compare Fig. 5_IV and 5_VIII). In both layers, the magnetic azimuth roughly follows the absorption features seen in the line cores of He I and H α , pointing mainly from sunspot a to sunspot b.

(2) The magnetic field strength decreases with height, with $B_{\text{chrom}}/B_{\text{phot}} \approx 0.5$. In the photosphere, the field strength within the emergence zone is between 300 G and 700 G, and exceeds 1800 G in sunspots. However, in the upper chromosphere, the field strength decreases to 850 G in the sunspots and declines to between 200 G (close to the detection threshold) and 400 G in the emergence zone.

(3) The magnetic structure in the emergence zone is more complex in the photosphere than in the upper chromosphere. Small patches of opposite polarity within the emergence zone are present in the photosphere (see Fig. 5_IV), whereas the transition from one polarity to the other is quite smooth in the chromosphere (Fig. 5_VIII). Figure 8a–c displays blowups of the emergence zone in the photosphere, showing the pixel-averaged vertical flux ($fB \cos \gamma$), absolute value of the magnetic field's inclination relative to the solar surface ($|\gamma - 90^\circ|$), and LOS velocity, respectively. The boxes mark the locations of features

identified with fluctuations in the inclination angle are indicative of bipolar structures. They appear similar to the moving dipolar features studied by Bernasconi et al. (2002) and features that are often found in EFRs studied by Hinode (e.g. Fig. 12 of Cheung et al. 2008). Here we prefer to refer to these features by their more general term magnetic bipolar features (MBFs). The polarity of an MBF close to a sunspot is found to always be opposite to that of the sunspot itself. The field of both polarities is inclined on average by 20° with respect to the solar surface. We cannot isolate MBFs from their surroundings based on LOS flows, although there is a tendency for there to be an upflow in one polarity and possibly a downflow in the other. The vertical magnetic field component in the upper chromosphere is plotted in Fig. 8d. It displays no sign of MBFs, indicating that MBFs are a purely photospheric phenomenon. They are indeed prominent features in the emergence site, Fig. 9 presenting a sequence of Stokes V images in which particularly prominent examples of MBFs are outlined by white rectangles. Many similar, but somewhat less distinctive MBFs, can also be detected in these and other similar images. The field of view of Fig. 9 is indicated by the $15 \text{ Mm} \times 15 \text{ Mm}$ dotted square in Fig. 6. The MBFs are elongated and aligned parallel to the absorption structures seen in the He I 10830 Å line core. No distinct separating motion between the two polarities of an MBF is observed during the 74 min over which the time series was recorded. If we track a particular MBF at the right-bottom corner of Fig. 9, we can roughly infer that the lifetime of MBFs can reach up to 45 min and the transversal motion is about 0.3 km s^{-1} . This result is comparable to the typical

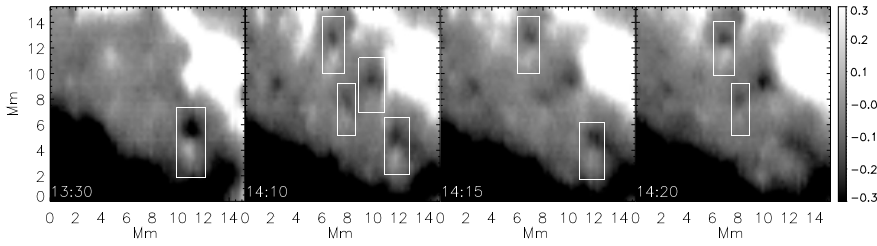


Fig. 9. Spatial maps of the Si I line Stokes V blue wing area, recorded at different times. The starting time of the plotted scans are 13:30 UT, 14:10 UT, 14:15 UT, and 14:20 UT, respectively. White (dark) patches indicate positive (negative) polarity. A number of MBFs are highlighted by white rectangles. The brightness of each panel is normalized to the maximum of the whole sequence. The field of view context is indicated by a dotted square in Fig. 6.

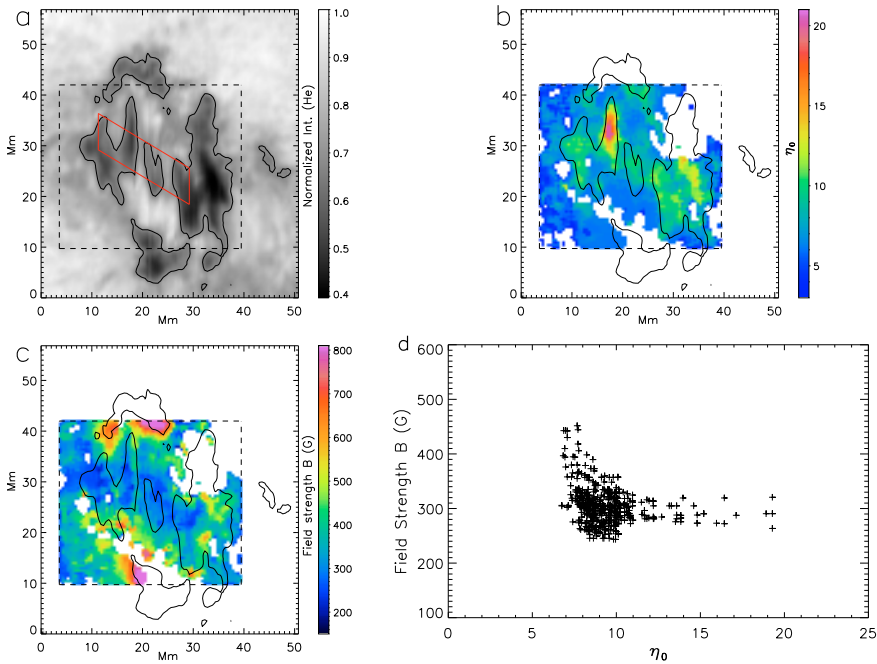


Fig. 10. a): intensity image of the He I line at 10830.3 Å. The dashed square outlines the region in which the parameter η_0 and the magnetic field strength are shown in panels b) and c) respectively. b): parameter η_0 retrieved from the best-fit profiles. c): retrieved magnetic field strength. Areas that either lie outside the region of interest or where a two-component model is needed have been left blank. d): scatter plot of the magnetic field strength versus the parameter η_0 . The plotted sample has been taken within the red trapezium overlaid onto panel a) (see text). The contour lines in panels a), b), and c) outline the absorption structures.

speed given by Bernasconi et al. (2002) using a 3.5 h long series of filtergrams. This speed is very close to the speed of sunspot b ($\leq 0.4 \text{ km s}^{-1}$, see Sect. 4.1), so that the motion of MBFs relative to that sunspot in our observation is too small to be detected.

5. Reconstruction of young loops in the upper chromosphere

We present the results of magnetic flux loops reconstructed following the method described by Solanki et al. (2003). The underlying assumption is that the He absorption follows a particular set of field lines produced by the high density of chromospheric material freshly emerging along the field indicated by the dark stripes in Fig. 5_V. It is evident that the He I line becomes optically thick along the loop-like structures. In Fig. 10a and b, we compare the maps of the intensity in the He I line core and the parameter η_0 , which is the ratio of the line core to continuum absorption coefficient. We find that η_0 becomes larger in the He dark loop-like structures, confirming a larger opacity there. The He line is also optically thick everywhere in the region where the loops are reconstructed. If we consider the area within the red trapezium in Fig. 10a, where the one-component model is valid and that cuts across the “tops” of various loops, we find that the magnetic field strength is anti-correlated with the optical thickness, η_0 , as quantitatively shown in Fig. 10d (We note that sunspot c lies outside the red trapezium). We note that $\eta_0 > 6$ for all the considered points, which implies that the He line core is optically thick. Since the field strength generally decreases with height, and we cannot “see” through the loop structures because

of their large optical thickness, we infer that the loop structures are located higher than their surroundings. In addition, we point out (without plotting) that there is no clear relationship between the field strength and optical thickness in the photosphere, also not, e.g., in sunspots in the chromosphere.

The loop is reconstructed by starting at one footpoint and tracking the direction of the magnetic vector there to determine the 3D coordinates of the field in the next pixel and so on, until the other footpoint is reached. In the present work, loops are traced based on the vector magnetic field in the local solar frame. In Fig. 11, we illustrate the traced loops as viewed from above (i.e., projected on the solar disk) and obliquely. The bundle of lines in the left panel, representing the traced magnetic field lines, follow the elongated absorption structures visible in He I (Fig. 5_V) relatively closely. In the right panel, the variation in LOS velocity and magnetic field strength along the traced field lines are represented by colors. The highest traced magnetic loops reach a height of almost 4 Mm from their footpoints at the “normal” level of He I 10830 Å line formation. We note that the z-axis scale in Fig. 11 is stretched and the loops are actually very shallow, as can be better judged from Fig. 12a, although the Z-axis is somewhat stretched even there.

The variation in atmospheric parameters along a typical loop is displayed in Fig. 12. The X-axis is the distance measured along the solar surface from the limb-side footpoint (having coordinates at $X = 18, Y = 15$ in the left panel of Fig. 11) to the other footpoint ($X = 22, Y = 42$). This loop is 25 Mm long and 3.5 Mm high. The magnetic field strength shows an asymmetric distribution and decreases by roughly a factor of 2 from

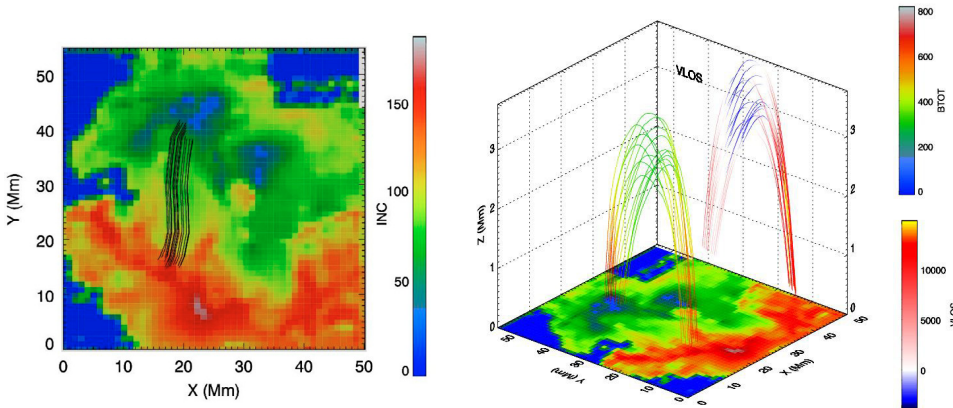


Fig. 11. Magnetic field structure of the loops reconstructed in an emerging flux region within NOAA 10917, based on the direct measurement of the magnetic vector in the upper chromosphere. *Left:* viewed directly from above. The chromospheric magnetic inclination map is overlaid by traced loops projected onto the solar disk. *Right:* the same, but viewed obliquely. The strength of the field along the traced field lines is color coded (upper color bar). The LOS velocity along the magnetic loop is color coded in the projection of the field lines onto the $Y-Z$ plane (lower color bar). Note that the Z -axis is stretched. Areas in dark-blue around the edge of the field of view are the regions where the polarization signals are below our fitting threshold.

loop footpoint to loop top (i.e. from 800 G /600 G to 300 G). The inclination angle changes smoothly along the loop, the field at the (chromospheric) footpoints still being rather inclined to the vertical. The azimuth exhibits a maximum deviation of 25° from the direction at the loop's apex (an azimuth angle of 90° refers to the direction parallel to the Y -axis of Fig. 11). The LOS velocity is asymmetric, an upflow with a peak value of nearly 3.8 km s^{-1} is found around the apex of the loop, the peak upflow being shifted to the disk-centerward side of the apex. The loop legs harbor stronger downflows, the faster downflow being seen along the limb side leg, where the field is weaker but also more aligned with the LOS. Co-existing supersonic and subsonic velocities (red and blue plus signs) are present along both loop legs. One can clearly see that the supersonic downflow speeds progressively increase toward the loop footpoints. The Stokes profiles along all the reconstructed loops mostly were well described by a single magnetic component, even where two velocity components were required. The reliability of the reconstructed magnetic structure is discussed in Sect. 6.3

6. Discussion

We have presented direct measurements of the vector magnetic field of an emerging flux region in the photosphere and upper chromosphere by the inverting Stokes profiles of the Si I and He I lines near 10830 \AA . This work is an extension of the analysis of Solanki et al. (2003) and Lagg et al. (2004, 2007) in that a second EFR is analyzed, which allows us, by comparing the properties, to judge which properties of the chromospheric field are common to EFRs and which are specific to a given region. It also extends those first results by employing the TIP II spectropolarimeter, which provides higher spectral and spatial resolution and a larger field of view than the original TIP. During the observations analyzed here, the slit also scanned the active region parallel to the AFS visible in $H\alpha$, so that the different parts of a given emerging magnetic loop were recorded at nearly the same time. Furthermore, the 180° ambiguity problem was resolved and the vector magnetic fields were transformed into the local solar frame by using a non-potential magnetic calculation technique (Georgoulis 2005).

In the following, we discuss some of the main results of in this paper.

6.1. Velocity field

In the upper chromosphere, the Doppler velocities are consistent with the expected motion in emerging flux loops, i.e. the material inside is draining along the loop, while the loop is ascending. Combining our repeated scans, we find that this motion lasts for more than 3 h, i.e. the length of time of the entire observation of long, dark structures in the He I line (13:24–16:51 UT). The long duration of the up- and down-flows implies that in the course of the observations we are witnessing different field lines passing through the upper chromosphere. Estimates of the drain time and rise time are given in Sect. 6.3. The Doppler velocity obtained from the He I line is rather similar to the velocities in AFS observed in $H\alpha$ (Bruzek 1967; Chou and Zirin 1988; Spadaro et al. 2004). Spadaro et al. (2004) studied the dynamic evolution of an AFS in a young active region ($\mu \approx 0.9$). They find $3\text{--}9 \text{ km s}^{-1}$ upflows at the tops of the AFS, and downflows of up to 17 km s^{-1} at the ends.

Significant supersonic downflows in the chromosphere, but only gentle subsonic flows in the photosphere, indicates that there has been a shock between the two layers, which agrees with the conclusion reached by Lagg et al. (2007) for NOAA 9451. In contrast to that region, however, no signs of emission in the He I lines is observed here, indicating that any heating due to the shock is restricted to layers below the formation level of the He I line. In the photosphere, the transversal velocity of the preceding sunspot b is $\leq 0.4 \text{ km s}^{-1}$. If we were to assume that the other footpoint is moving at the same speed, then the transversal motion would be a factor of 10 smaller than the upflows measured at the loop tops, which suggests that the emerging loops expand much more rapidly in the vertical direction than in the horizontal.

6.2. Magnetic fields

The freshly emerged magnetic field has a similar inclination-field strength relationship in the photosphere and upper chromosphere. In both layers, the vector field is weak and horizontal within the emergence zone. It becomes stronger and more vertical when moving toward the edges of this zone. A linear relation is found between field strength and inclination to the vertical. For the photosphere, this agrees with the results of Lites et al. (1998), but also Stanchfield et al. (1997) and Solanki (2003) for

sunspots. The magnetic field strength decreases with height. The photospheric field strength within the emergence zone lies between 300 G and 700 G, and exceeds 1800 G in sunspots. Brants (1985b) and Lites et al. (1998) obtained similar field strength from the Fe I 6302.5 Å and 6301.5 Å/6302.5 Å line pair, respectively. In the upper chromosphere, the field strength decreases to 850 G in the sunspots or pores and even falls to 200 G in the emergence zone, which is compatible with the first measurement by Solanki et al. (2003). Assuming that the average distance between the normal Si I and He I formation heights is $\Delta Z = 1000\text{--}1500$ km (Schmidt et al. 1995; Centeno et al. 2006; Bloomfield et al. 2007), the vertical gradient of spatially averaged field strength dB/dZ is in the range $0.1\text{--}0.2$ G km $^{-1}$ within the emergence zone and around $0.3\text{--}0.6$ G km $^{-1}$ within the sunspots at the loop footpoints. The average vertical gradient inside sunspots is similar to other measurements for a large sunspot (Rüedi et al. 1995; Orozco et al. 2005), who found that dB/dz varies from $0.4\text{--}0.6$ G km $^{-1}$ in the umbra to $0.1\text{--}0.3$ G km $^{-1}$ in the outer penumbra. The authors used the same lines as us and assumed an equivalent height range. We note that here we obtained these gradients for sunspots without taking into account the older sunspot d and newly born sunspot c. It is of interest that the older sunspot d, present already before the new flux started to emerge, is clearly visible as a strong azimuth center in the photosphere (Fig. 5_III), but not in the upper chromosphere (Fig. 5_VII). This is also true prior to the conversion to local solar coordinates, so that it cannot be an artifact of the 180° ambiguity. The field strength in sunspot d falls from 1600 G in the photosphere to 400 G in the upper chromosphere, the dB/dZ almost reaching 0.8 G km $^{-1}$ (for a $\Delta Z = 1500$ km). It appears that the freshly emerging loops have expanded strongly sideways and partly overlie the previously present sunspot. Given the strength of the field of other sunspots in the chromosphere, this is a surprising result and indicates that the field in the chromosphere above this sunspot is measured at a considerable height since the field strength above this sunspot is not significantly higher than in its surroundings, quite unlike sunspots a and b. The field above sunspot c is similarly weak in the chromosphere. In this case, He I filaments are clearly seen to cross this spot, supporting the idea that the weak fields seen above this spot are caused by the filaments crossing it.

All vertical field strength gradients determined here must be considered with some caution, since 1500 km represents an upper limit to the vertical height separation – see Sects. 5 and 6.3. The gradient is also affected by the straylight. Because of the far greater inhomogeneity of the field in the photosphere than in the chromosphere, straylight has a stronger influence on the spatial distribution of the photospheric field strength than on that of in the chromosphere. This means that in general the gradient will be lower in regions of strong field, such as sunspot umbrae. The effect of straylight in sunspots is greater because the sunspots appear dark in the photosphere, but not particularly so in the chromosphere. Hence the influence of straylight from their bright surroundings is enhanced, making the field strength appear lower in the photosphere.

A rough and grossly simplified sketch of the magnetic structure of the EFR inferred from the present work is given in Fig. 13. It illustrates the difference between the complex magnetic structures in the photosphere and the comparatively simple structures in the upper chromosphere. Solanki et al. (2003) noted a similar difference in the complexity of the fields in the photosphere and chromosphere. Thus, they observed “localized patches of opposite-polarity fields within the larger scale unipolar regions”. The higher resolution of the present work identifies

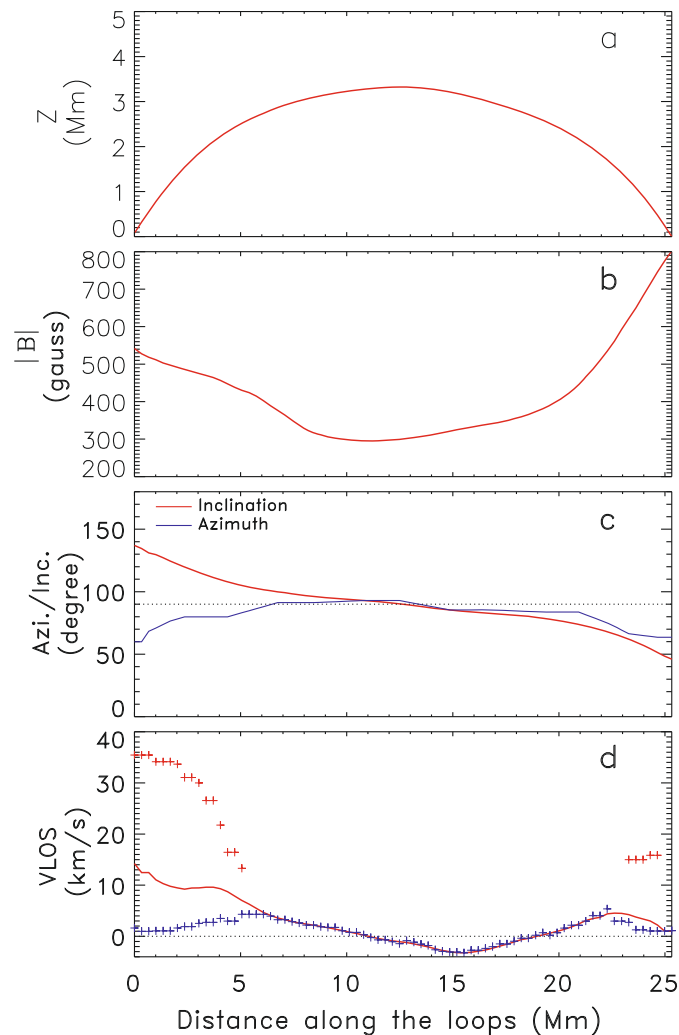


Fig. 12. a)–d): variation in the atmospheric parameters along a typical reconstructed loop. The X-axis is the distance measured along the solar surface below the loop from one footpoint (located at $X = 18$, $Y = 15$) to the other footpoint ($X = 22$, $Y = 42$). a): height of the loop vs. distance (note the stretched Z axis). b): magnetic field strength. c): field direction. The inclination is given in red and the azimuth in blue. The dotted-line represents the 90° inclination angle (polarity reversal). d): the filling-factor weighted LOS velocity (red solid line). Co-existing atmospheric components with different LOS velocity are represented by plus symbols. The fast component is in red and the slow component in blue. The dotted line indicates zero LOS velocity, downflows corresponding to positive velocities.

many of these feature to be bipolar. Small magnetic bipolar features (MBFs) are only present in the photosphere and clearly do not reach the upper chromosphere. The polarity of an MBF close to the nearest sunspot is always opposite to that of the sunspot itself. The field is close to being horizontal to the solar surface, the angle being on average 20°. The appearance of these features is in good qualitative agreement with the observation of emerging flux regions by Hinode (e.g. Fig. 12 of Cheung et al. 2008; Fig. 2 of Magara 2008), and is reflected in the most realistic MHD simulations (Cheung et al. 2007). In addition, our observation indicates that the two parts of MBFs remain connected for the duration of our 74 min observation. These features may be related to the moving dipolar features (MDFs) that were first reported and named by Bernasconi et al. (2002), but it is difficult to determine the relative motion of MBFs toward

the nearest sunspot from our observations. Our data support the proposal of Bernasconi et al. (2002) that the magnetic configuration of these features corresponds to U-loops. This explanation is consistent with the absence of MBFs in the upper chromosphere. U-loops also explain the continuing proximity of the two poles over the full life time of an MBF, which varies from tens of minutes to hours according to Bernasconi et al. (2002). If we try to reconcile the chromospheric and photospheric magnetic structures with “simple” chromospheric loops constantly rising and becoming replenished while the photospheric field maintains its convolved structure, we must find a way for the magnetic field to remove the U-loops before it rises into the chromosphere and eventually into the corona. One possibility is that magnetic reconnection at the top of the U-loop forms an O-loop and an overlaying Ω -loop. This process is illustrated in Fig. 14. The overlying “simple” loop then expands into the chromosphere and eventually into the corona, while the O-loop dissipates. If this scenario is correct then some of the MBFs many actually be O-loops that developed out of U-loops.

6.3. The reconstructed magnetic loops

The emerging young magnetic loops are reconstructed in the upper chromosphere in the local solar frame. They are morphologically well aligned with long dark structures visible in the He I 10 830 Å and H α lines (the arch filaments). Compared with loops previously traced by Solanki et al. (2003), the present loops are more shallow and horizontal. On average, they have a footpoint separation of 25 Mm and are 3 Mm high, while the reconstructed loops in NOAA 9541 had a footpoint separation of 20 Mm and were 10 Mm high. In the present EFR, we do not find any evidence of a current sheet.

Judge (2009) estimated the drain time of the loops studied by Solanki et al. (2003), using the measured dimensions and Doppler velocities. He argued that it is probable that these loops had been almost completely drained by the time of the observations. We now perform a similar order-of-magnitude estimation for the loop system studied in this paper. Since the loops are nearly horizontal, the arc length of the loops is roughly equal to the distance between the two footpoints, $L = 25$ Mm. The mean draining velocity, v_d , is around 10 km s^{-1} . Assuming that mass is conserved, we have $t_d \approx L/2v_d = 25\,000 \text{ km}/20 \text{ km s}^{-1} \approx 1200 \text{ s} \approx 20$ min. This is consistent with the observation that the lifetime of individual AF in H α is about 10–30 min (Chou 1993). Given the loop height of 3 Mm, the rise time is around $h/v_u \approx 3000 \text{ km}/4 \text{ km s}^{-1} \approx 750 \text{ s}$ (h = loop height, v_u = rise speed). Thus the magnetic loops still carry excess material and hence they can appear as regions of excess absorption in He I (i.e. as an AFS). We note that the strength of the He line in the loops may be only partly related to a higher density. It may also be caused by the loop being immersed in the hot corona. The stronger irradiation by EUV flux (coming from all sides) leads to higher ionization and greater recombination of He, so that the He 10 830 Å triplet becomes stronger.

The observed loop reflects the asymmetric distribution of both the magnetic field and LOS velocity. Since we scanned the region with the slit parallel to the AFS seen in H α , we can exclude this result being caused by observing different sides of loops at different times. We explain the LOS velocity asymmetry as follows. Firstly, we found that the upflow peak is in the disk-centerward side as shown in Fig. 12d, which is consistent with a loop that is expanding as it rises (indicated by the 3 blue arrows in Fig. 13). Secondly, the loop-leg LOS velocity on the limb side

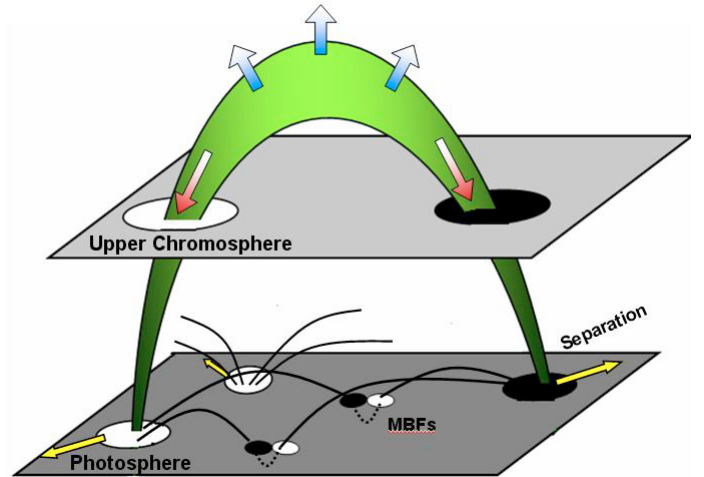


Fig. 13. Sketch of the magnetic field structure in an emerging flux region, summarizing the main observed features. The lower plane represents a cut at the photospheric level, the upper plane at the average chromospheric level. The white (dark) points signify positive (negative) polarity. The green arch connecting the opposite polarities represents an emerging magnetic loop going through the photosphere into the upper chromosphere. The color of the arch indicates the magnetic field strength (deep color corresponds to a strong magnetic field). The arrows in blue and red represent the upflows and downflows detected in the upper chromosphere, respectively. In the photosphere, the footpoints with opposite polarity move apart from each other, as indicated by the yellow arrows. The MBFs, present in the emergence zone, are represented by small pairs of white/black patches. A U-type loop represents the MBF magnetic field configuration. An isolated white patch represents the old sunspot, present already before the new flux started to emerge. It is partly covered by loops of freshly emerging flux. Solid (dotted) lines represent the magnetic field lines above (under) the photosphere.

is almost a factor of 2 larger than on the disk-centerward side. We assume that the true velocity is along the direction of the local magnetic field, hence $V_{\text{los}} = V \cos \alpha$ (here V is the true velocity at the footpoints, α is the angle between the LOS and the magnetic field, and we neglect the motion of the field itself). We note that the angle between the local vertical and the LOS is about 30° according to the heliocentric position of this EFR. From Fig. 12, we therefore inferred that the α on the disk-centerward side is about 75° ($= 45^\circ + 30^\circ$) and about 170° ($= 140^\circ + 30^\circ$) on the limb side. Hence the fast component of V_{los} is about 16 km s^{-1} on the disk-centerward side and 36 km s^{-1} on the limb side. We infer that the true velocity in the disk-centerward side can reach 60 km s^{-1} and is higher than that in the limb side by a factor of 1.7.

Judge (2009) questioned that the He I 10 830 Å can be used to reconstruct the loop geometry. He argued that the field in these structures is measured at a nearly constant height, instead of along a magnetic loop. However, there are strands of evidence that support the interpretation put forward by Solanki et al. (2003) and in this paper:

- (a) From the intensity image, we observe a general similarity between the AFS seen in the H α and He I 10 830 Å lines. In particular, the He I absorption structures are smooth and elongated, like the H α arch filaments (see Figs. 2c and d), and rather distinct from the more mottled character of the structures seen in, e.g., the Ca II K line, strongly indicating

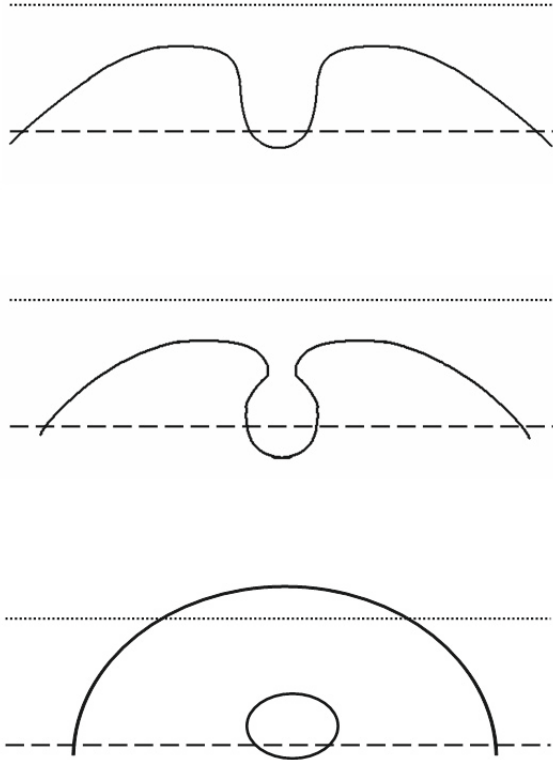


Fig. 14. Sketch of the evolution of a pair of emerging magnetic loops connected below the surface by a U-loop. As the loops rise, they can reconnect above the U-loop, leaving an O-loop and an overlying Ω loop. Time runs *from top to bottom*. The dashed line represents the solar surface, the dotted line the level above which He 10 830 Å is formed.

that the He I absorption indeed follows individual emerging flux loops (like H α), rather than sampling only their footpoints (like Ca II K). Even Ca II K reveals elongated filaments in plage if observed at sufficiently high resolution (Pietarila et al. 2009), suggesting that its emission also follows magnetic field lines to some extent.

(b) The chromospheric field strength above sunspot c (which has very recently emerged) is excessively small, implying that there is either a much higher dB/dZ than above other spots, or that we measure the field at a greater height than above the spots a and b. The second interpretation is consistent with the presence of dark He filaments passing over spot c. The magnetic field there is more or less horizontal i.e. inclined by 70–80° on average with respect to the local vertical direction.

(c) In the emergence zone, the He I line becomes optically thick in the loop-like structures and the magnetic field strength is anti-correlated with the opacity. This suggests that we observe higher layers in the loops since the field strength decreases with height.

(d) An example of scattering polarization in Stokes Q and U located around the loop top is shown in Fig. 4. The combined amplitude of $\sqrt{Q^2 + U^2}/I_c$ is 0.22%. Scattering polarization signals of such a large amplitude are found only around loop tops. The scattering polarization signal is enhanced when the anisotropy of the radiation field increases, i.e. with height. Asensio Ramos et al. (2008) pointed out that it is possible to retrieve reliable height information and the full magnetic vector simultaneously if one parameter of the magnetic field

vector is known beforehand. For example, if one such parameter can be constrained by the Zeeman effect, then the height information can be retrieved. In Fig. 4, we clearly see the joint action of Zeeman and Hanle effects and perform a HeLIx⁺ inversion (Lagg et al. 2009) to infer the height of formation of the He I scattering polarization at this location. HeLIx⁺ is an upgraded version of HeLIx (Lagg et al. 2004) that includes the forward modeling calculation core of the computer program HAZEL of Asensio Ramos et al. (2008), which is based on the quantum theory of the Hanle and Zeeman effects (see Landi Degl’Innocenti & Landolfi 2004). We employed a one-component, constant-property slab atmosphere (Trujillo Bueno et al. 2005; Asensio Ramos et al. 2008) with the free parameters of magnetic field strength B , inclination and azimuth angle, γ and χ , Doppler velocity v_{los} , the damping constant a , the optical thickness of slab τ_{slab} , and the height of the slab above the solar surface h_{slab} . To obtain reliable error estimates for the retrieved atmospheric parameters, we repeated the inversion of this particular pixel 100 times. Due to the random walk convergence of the Pikaia algorithm (Charbonneau 1995), the variations in the retrieved parameter values for the individual runs contain all possible sources of errors during the inversion process, including those caused by the degeneracy between some parameters. Comparisons of these error estimates with those of the Bayesian technique described by Asensio Ramos et al. (2007) showed good agreement. The standard deviation of the field direction is very small, $\chi \approx 72^\circ \pm 0.5^\circ$, $\gamma \approx 112^\circ \pm 0.4^\circ$, the optical depth in the red-blended component being $\Delta\tau = 1.0 \pm 0.19$. From the set of 100 inversions, we deduced $h_{\text{slab}} \approx 7.1 \pm 2.0$ arcsec from the solar surface. Hence, the loop top should be higher than 3.6 Mm above the photosphere (1σ). The average height of the loop obtained from our geometrical reconstruction is around 3 Mm above the normal He formation height of 1–1.5 Mm, resulting in a total height of 4–4.5 Mm above the solar surface, which is consistent with the scattering polarization diagnostics. However, the reliability of the inferred height information using this technique needs to be discussed further. More details on this technique and more evidence of the greater height of the loops compared to the claims of Judge (2009) are presented by Merenda et al. (in preparation).

In summary, many arguments support our interpretation that the He I 10 830 Å line allows cool loops that have freshly emerged in the EFR to be traced in 3D.

7. Conclusions

After NOAA 9451 studied by Solanki et al. (2003) and Lagg et al. (2004; 2007), NOAA 10917 is only the second EFR whose velocity and vector magnetic field have been investigated in both the solar photosphere and chromosphere. Both regions display considerable similarities. Their images in He I 10 830 Å exhibit arch filament systems comparable to those seen in H α . The magnetic field is found to follow the He filaments in the shape of a loop. These chromospheric loops are relatively low lying, having a lower apex height than the chromospheric loops in NOAA 9451.

Both active regions exhibit a remarkable difference in the complexity of their photospheric and chromospheric magnetic structures. Whereas the chromospheric structure is comparatively simple, being dominated by the low-lying loops and the fields of spots and pores, in the photosphere a considerable

amount of additional magnetic structures are found in the middle of the EFR. We identify these features with compact bipolar features and interpret them as being U- or possibly O-loops. They are similar to structures seen by Hinode/SOT/SP in EFRs.

Acknowledgements. The data used in this paper were obtained with the German Vacuum Tower Telescope in the Teide Observatory of Spain. The authors thank A. Pietarila, T. Wiegmann, and C. Sasso for very helpful discussions and comments, which led to improvements of the work. This work was partly supported by the National Natural Science Foundation grant 10933003 of China, and by WCU grant No. R31-10016 funded by the Korean Ministry of Education, Science and Technology.

References

- Andretta, V., & Jones, H. P. 1997, *ApJ*, 489, 375
- Asensio Ramos, A., & Martínez González, M. J. & Rubiñ-Martin, J. A. 2007, *A&A*, 476, 959
- Asensio Ramos, A., Trujillo Bueno, J., & Landi Degl'Innocenti, E. 2008, *ApJ*, 683, 542
- Avrett, E. H., Fontenla, J. M. & Loeser, R. 1994, in *Infrared Solar Physics*, ed. D. M. Rabin (Dordrecht:Kluwer), IAU Symp., 154, 35
- Aznar Cuadrado, R., Solanki, S. K., & Lagg, A. 2005, in *Chromosphere and Coronal Magnetic Fields*, ed. D. E. Innes, A. Lagg, & S. K. Solanki, ESA SP-56, 49
- Aznar Cuadrado, R., Solanki, S. K., & Lagg, A. 2007, in *Modern Solar Facilities-Advance Solar Science*, ed. F. Kneer, K. G. Puschmann, & A. D. Wittmann (Universitätsverlag Göttingen), 173
- Beck, C., Schlichenmaier, R., Collados, M., Bellot Rubio, L., & Kentischer, T. 2005, *A&A*, 443, 1047
- Bernasconi, P. N., Rust, D. M., & Georgoulis, M. K., et al. 2002, *Sol. Phys.*, 209, 119
- Bloomfield, D. S., Lagg, A., & Solanki, S. K. 2007, *ApJ*, 671, 1005
- Brants, J. J. 1985a, *Sol. Phys.*, 95, 15
- Brants, J. J. 1985b, *Sol. Phys.*, 98, 197
- Bruzek, A. 1967, *Sol. Phys.*, 2, 451
- Bruzek, A. 1969, *Sol. Phys.*, 8, 29
- Caligari, P., Moreno-Insertis, F., & Schüssler, M. 1995, *ApJ*, 441, 886
- Caligari, P., Schüssler, M., & Moreno-Insertis, F. 1998, *ApJ*, 502, 481
- Centeno, R., Collados, M., & Trujillo Bueno, J. 2006, *ApJ*, 640, 1153
- Centeno, R., Socas-Navarro, H., & Lites, B., et al. 2007, *ApJ*, 666, L137
- Centeno, R., Trujillo Bueno, J., Uitenbroek, H., & Collados, M. 2008, *ApJ*, 677, 742
- Charbonneau, P. 1995, *ApJS*, 101, 309
- Cheung, M. C., Schüssler, M., & Moreno-Insertis, F. 2007, *A&A*, 467, 703
- Cheung, M. C., Schüssler, M., Tarbell, T. D., & Title, A. M. 2008, *ApJ*, 687, 1373
- Chou, D. Y. 1993, in *The Magnetic and Velocity Fields of Solar Active Regions*, ASP Conf. Ser. 46, ed. H. Zirin, G. Ai, & H. Wang, IAU Colloq., 141, 471
- Chou, D. Y., & Zirin, H. 1988, *ApJ*, 333, 420
- Collados, M., Trujillo Bueno, J., & Asensio Ramos, A. 2003, in *Solar Polarization 3*, ed. J. Trujillo Bueno, & J. Sánchez Almeida, ASP Conf. Ser., 307, 468
- Collados, M., Lagg, A., & Díaz García, J. J., et al. 2007, in *The Physics of Chromospheric Plasmas*, ed. P. Heinzel, I. Dorotović, & R. J. Rutten, ASP Conf. Ser., 368, 611
- Delaboudinière, J. -P., Artzner, G. E., Brunaud, J., et al. 1995, *Sol. Phys.*, 162, 291
- Fan, Y. 2004, *Living Rev. Solar Phys.*, 1 <http://solarphysics.livingreviews.org/Articles/lrsp-2004-1/>
- Georgoulis, M. K. 2005, *ApJ*, 629, L69
- Harvey, K., & Harvey, J. 1973, *Sol. Phys.*, 28, 61
- De Jager, C., Namba, O., & Neven, L. 1966, *Bull. Astron. Inst. Netherlands*, 18, 128
- Judge, P. G. 2009, *A&A*, 493, 1121
- Kubo, M., Shimizu, T., & Lites, B. W. 2003, *ApJ*, 595, 465
- Landi Degl'Innocenti, E. 1982, *Sol. Phys.*, 79, 291
- Landi Degl'Innocenti, E., & Landolfi, M. 2004a, *Polarization in Spectral lines* (Dordrecht: Kluwer)
- Lagg, A. 2007, *Adv. Space Res.*, 39, 1734
- Lagg, A., Woch, J., Krupp, N., & Solanki, S. K. 2004, *A&A*, 414, 1109
- Lagg, A., Woch, J., Solanki, S. K., & Krupp, N. 2007, *A&A*, 462, 1147
- Lagg, A., Ishikawa, R., & Merenda, L., et al. 2009, in *Second Hinode Science meeting: Beyond Discovery-Toward Understanding*, ed. B. Lites, M. Cheung, T. Magara, J. Mariska, & K. Reeves, ASP Conf. Ser., 415, 327
- Lee, J. W. 1992, *Sol. Phys.*, 139, 267
- Lin, H., Penn, M. J., & Kuhn, J. R. 1998, *ApJ*, 493, 978
- Lites, B. W., Skumanich, A., & Martínez Pillet, V. 1998, *A&A*, 333, 1053
- Magara, T. 2008, *ApJ*, 685, L91
- Martínez González, M. J., & Bellot Rubio, L. R. 2009, *ApJ*, 700, 1391
- Martínez González, M. J., Collados, M., Ruiz Cobo, B., & Solanki, S. K. 2007, *A&A*, 469, 39
- Martínez Pillet, V., Lites, B. W., & Skumanich, A. 1998, in *Crossroads for European Solar and Heliospheric Physics*, ed. R. Harris, F. Moreno Insertis, & E. Priest, ESA SP-417, 259
- Merenda, L., Trujillo Bueno, J., Landi Degl'Innocenti, E., & Collados, M. 2006, *ApJ*, 642, 554
- Metcalfe, T. R., Leka, K. D., Barnes, G., et al. 2006, *Sol. Phys.*, 237, 267
- November, L. J., & Simon, G. W. 1988, *ApJ*, 333, 427
- Orozco Suárez, D., Lagg, A., & Solanki, S. K. 2005, *Chromosphere and coronal magnetic field*, ed. D. E. Innes, A. Lagg, S. K. Solanki, & D. Danesy, ESA-SP-596, 51
- Penn, M. J., & Kuhn, J. R. 1995, *ApJ*, 441, L51
- Pietarila, A., Hirzberger, J., Zakharov, V., & Solanki, S. K. 2009, *A&A*, 502, 647
- Pozhalova, Z. A. 1988, *Soviet Ast.*, 65, 1037
- Rüedi, I., Solanki, S. K., & Livingston, W. C. 1995, *A&A*, 293, 252
- Rüedi, I., Keller, C. U., & Solanki, S. K. 1996, *Sol. Phys.*, 164, 265
- Sasso, C., Lagg, A., & Solanki, S. K. 2006, *A&A*, 456, 367
- Scherrer, P. H., Bogart, R. S., Bush, R. I., et al. 1995, *A&A*, 162, 129
- Schüssler, M., Caligari, P., Ferriz-Mas, A., & Moreno-Insertis, F. 1994, *A&A*, 281, 69
- Schmidt, W., Knölker, M., & Westendorp-Plaza, C. 1995, *A&A*, 287, 299
- Schmieder, B., Rust, D. M., Georgoulis, M. K., Démoulin, P., & Bernasconi, P. N. 2004, *ApJ*, 601, 530
- Socas-Navarro, H., & Uitenbroek, H. 2004, *ApJ*, 603, L129
- Socas-Navarro, H., Trujillo Bueno, J., & Landi Degl'Innocenti, E. 2004, *A&A*, 612, 1175
- Solanki, S. K. 2003, *A&ARv*, 11, 153
- Solanki, S. K., & Steiner, O. 1990, *A&A*, 234, 519
- Solanki, S. K., Lagg, A., Woch, J., Krupp, N., & Collados, M. 2003, *Nature*, 425, 692
- Spadaro, D., Billotta, S., Contarino, L., Romano, P., & Zuccarello, F. 2004, *A&A*, 425, 309
- Stanchfield, D. C. H., Thomas, J. H., & Lites, B. W. 1997, *ApJS*, 477, 485
- Strous, L. H., & Zwaan, C. 1999, *ApJ*, 527, 435
- Strous, L. H., Scharmer, G., Tarbell, T. D., Title, A. M., & Zwaan, C. 1996, *A&A*, 306, 947
- Trujillo Bueno, J. 2009, in *Magnetic Coupling between the Interior and the Atmosphere of the Sun*, ed. S. S. Hasan, & R. J. Rutten, *Astrophys. Space Sci.* (Berlin: Springer-Verlag), in press
- Trujillo Bueno, J., & Asensio Ramos, A. 2007, *ApJ*, 655, 642
- Trujillo Bueno, J., Landi Degl'Innocenti, E., Collados, M., Merenda, L., & Manso Sainz, R. 2002, *Nature*, 415, 403
- Trujillo Bueno, J., Merenda, L., Centeno, R., Collados, M., & Landi Degl'Innocenti, E. 2005, *ApJ*, 691, 191
- Zhang, J., Solanki, S. K., & Wang, J. X. 2003, *A&A*, 399, 755
- Zwaan, C., & Brants, J. J. 1985, *Sol. Phys.*, 95, 3